1

Turbulence-Resilient Reflective Fi-Wi-Fi Bridge for Terrestrial Free-Space Optical Data Links

Florian Honz, Student Member, IEEE, and Bernhard Schrenk, Member, IEEE

Abstract—Free-space optical (FSO) links enable a seamless extension of the fiber-grade bandwidth continuum in fiber-scarce environments. Towards this, we present a bidirectional fiberwireless-fiber link that bridges the gap between two single-mode fiber ports. We utilize simple focal plane array beamformers that host 91 antenna elements on a fiber tip to ensure the optimal coupling of light in terrestrial point-to-point FSO links, for which hybrid space / wavelength-switched beamforming networks are employed to enable centralized control. The asymmetric complexity distribution in the FSO link layout is further enhanced through a reflective, source-less tail-end equipment and wavelength re-use to accomplish full-duplex 10 Gb/s data transmission with simultaneous channel sounding in an adjacent waveband. Moreover, we propose and demonstrate a graceful migration path towards diversity reception through simple wavelength-set coding, which enables us to mitigate the effect of turbulence-induced signal fading on the data transmission.

Index Terms—Free-space optical communication, Optical communication terminals, Optical antennas, Optical turbulence

I. INTRODUCTION

PTICAL wireless communication (OWC) is a license-free high-bandwidth alternative to radio frequency (RF) based over-the-air communications. It supports operation in environments that are contaminated by electro-magnetic interference and can serve as a cost-effective replacement of optical fiber for temporary installations [1]. OWC has been considered for a number of attractive application domains, such as in-door access [2], underwater communications [3], inter-satellite and satellite-to-ground communications [4] and terrestrial free-space optical (FSO) backhaul links [5, 6, 7]. Furthermore, OWC has been demonstrated in scenarios that involve mobile users, including ships [8], aerial vehicles [9] and space probes, through the latter demonstrating the FSO-enabled streaming of an ultrahigh-definition video at a data rate of up 267 Mb/s over a distance of 30 million kilometers or 0.2 astronomical units [10].

The uncontended bandwidth performance of optical wireless links often comes at a considerable complexity burden, which often spoils their cost-effective deployment. On

Manuscript received June 25, 2025. This work has received funding from the Smart Networks and Services Joint Undertaking (SNS JU) under the European Union's Horizon-Europe research and innovation programme under Grant Agreement No. 101139182.

F. Honz and B. Schrenk are with the AIT Austrian Institute of Technology, Center for Digital Safety & Security, Giefinggasse 4, 1210 Vienna, Austria (phone: +43 50550-4185; e-mail: florian.honz@ait.ac.at).

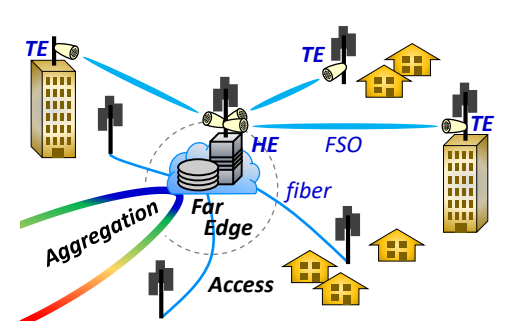


Fig. 1. Integration of FSO links for local access and x-haul in fiber-scarce environments.

top of this, out-door FSO links are challenged by atmospheric effects and potentially poor weather conditions. A practical FSO link therefore not only requires pointing, acquisition and tracking to establish and maintain the link, but also means to mitigate signal fading due to turbulence [11]. Towards this direction, earlier works have proposed receiver-side photonic multiple-input / multiple-output processors and digital signal processing (DSP) methods such as selective- or maximumratio combining of received modes [12-17]. Since demonstrations such as in [12] are terminating the FSO link rather than providing a transparent Fi-Wi-Fi link, they are suitable only for translucent links. Others, such as [13], employ DSP in combination with coherent signal transmission, thus rendering it specific to the modulation and coding scheme, also questioning whether mitigation on a persignal level can be more efficient than a joint method addressing the entire FSO link. [14], [15] and [16] alternatively employ few- and multi-mode fibers, which trade bidirectionality of the FSO link against robustness of a unidirectional link. The use of larger-core fiber further introduces restrictions for the end-to-end link bandwidth if transmission over a Fi-Wi-Fi bridge with continued lightpath is considered.

This paper extends our initial study [18] on a bidirectional fiber-wireless-fiber (Fi-Wi-Fi) bridge and demonstrates a bidirectional point-to-point FSO link that connects two single-mode ports through focal plane array (FPA) beamformers that host 91 antenna elements on a fiber tip. We experimentally demonstrate centralized beamforming control through a hybrid space- / wavelength-switched FPA architecture in a reflective FSO link configuration that supports full-duplex 10 Gb/s transmission by means of wavelength re-use and simultaneous channel sounding. We further prove a graceful diversity-reception upgrade for the FSO bridge to effectively mitigate

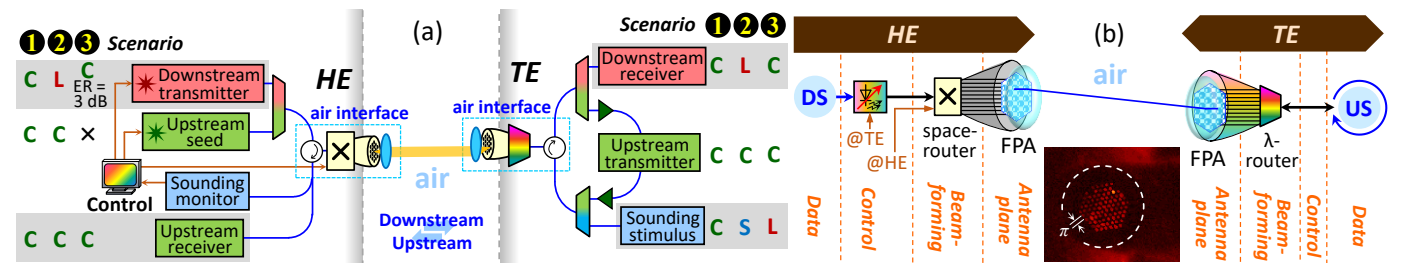


Fig. 2. (a) Link-level architecture of the bidirectional FSO link, together with the spectral allocation according to the different implementation scenarios of the Fi-Wi-Fi bridge. (b) Optical beamforming methodology and control for the bidirectional FSO link.

TABLE I
FI-WI-FI BRIDGE IMPLEMENTATION SCENARIOS
AND USE OF OPTICAL SPECTRUM.

FSO configuration	DS	US	Sounding
1 Half-duplex	C-band, ER > 10 dB	C-band	C-band, periodic
2 Full-duplex with paired spectrum	L-band, ER > 10 dB	C-band	S-band, continuous
Full-duplex through λ re-use	C-band, ER = 3 dB	C-band	L-band, continuous

optical turbulence through simple wavelength-set data coding. As a result, the proposed design omits the need for complex DSP, elaborate photonic circuit designs, fast beam steering mirrors or multimode fibers to mitigate turbulence, while also enabling bidirectional link operation.

Compared to our previous study [19], introducing the beamforming and Fi-Wi-Fi concept, this paper demonstrates an increased number of optical antenna elements for an enhanced field-of-view as well as simultaneous S-band sounding. This enables novel bidirectional operation via the C-and L-bands, together with simultaneous sounding. In addition, this study demonstrates simple and effective turbulence mitigation. While our initial study [18] demonstrates the core concept, this paper extends it by providing a detailed analysis on the loss contributions from the constituent beamforming elements and wavelength-specific performance aspects, as well as an investigation on the cyclic behavior of wavelength-routed FPA beamformers, including a tailored multi-band 8×8 AWG. Furthermore, we provide a detailed characterization of the induced turbulence.

The manuscript is organized as follows. Chapter II presents the concept of a Fi-Wi-Fi bridge with asymmetric complexity distribution and the adopted methods for beamforming, remote control / modulation and channel sounding. Chapter III highlights the experimental evaluation setting, while Chapter IV characterizes the FSO link. Chapter V then discusses the data transmission performance in three selected scenarios. Chapter VI eventually demonstrates the mitigation of atmospheric turbulence. Finally, Chapter VII concludes the work.

II. BIDIRECTIONAL REFLECTIVE FSO LINK

The FSO link considered in the following investigation aims at an asymmetric complexity distribution among its terminals, as it would apply for optical wireless links that connect aggregating nodes in a local access network setting towards its end-points [20]. Such a configuration is sketched in Fig. 1, where FSO supports a bandwidth continuum between the far edge and distributed network units in fiber-scarce environments. Towards this, the support of a fiber-grade continuum over FSO can be considered as a formidable challenge as it requires to reliably couple light between to single-mode fiber ports. In general, various application scenarios for short range FSO links, ranging from simple inter-building point-to-point connections to local cloud-based radio access network applications can be envisioned [21].

The architecture of such a bidirectional FSO link is proposed in Fig. 2(a). It is laid out as a Fi-Wi-Fi bridge that leverages FPA beamformers at the head-end (HE) and tail-end (TE) FSO terminals to accomplish alignment tolerance and turbulence mitigation. Moreover, its resource partitioning follows a centralized approach through reflective upstream modulation and optical beamforming methods specific to the FSO terminals. The FSO link has been evaluated in three different scenarios, which are listed in Table 1. These scenarios investigate various complexity / performance tradeoffs when implementing the FSO link with respect to its duplexing methodology, its monitoring and control functions and its use of spectral resources.

Specifically, scenario exclusively employs a C-band setup for half-duplex 10 Gb/s on-off keyed downstream (DS) and upstream (US) transmission, which is performed together with periodic channel sounding interleaved to the data transmission. Scenario dedicates entire bands to DS (L-band) and US (C-band) transmission as well as channel sounding (S-band). With this, it facilitates full-duplex data transmission while it evaluates the FSO link quality simultaneously. Scenario simplifies this spectral layout by introducing wavelength-reuse for the purpose of full-duplex DS/US transmission in the C-band. For this purpose, a reduced extinction ratio (ER) of 3 dB is set for the intensity-modulated DS, which enables the TE to re-cycle the DS signal as optical carrier for its remodulation with US data [22]. Channel sounding is continuously performed at the now unoccupied L-

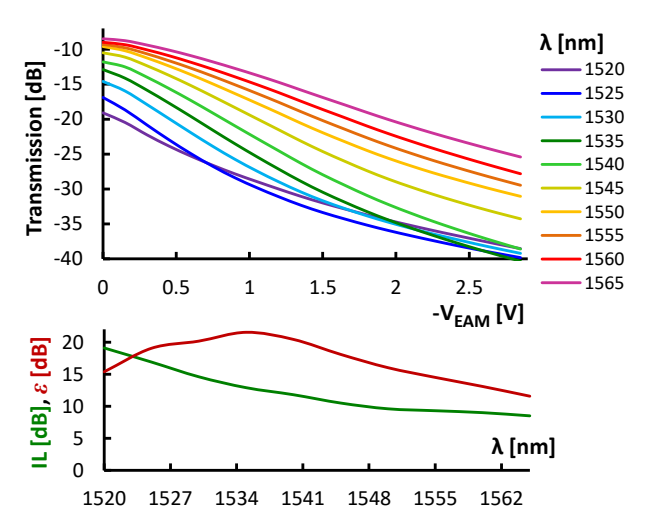


Fig. 3. Optical transmission of the EAM and wavelength-specific loss and extinction ratio.

band. The overall use of spectrum is therefore compressed to two wavebands.

By design, scenarios 2 and 3 do not maximize the spectral efficiency, as it is paramount for metro-core deployments, since they target access-like network deployments where usually a bidirectional full-duplex link utilizing two optical carries is used. This offers simplicity while also freeing up resources for turbulence mitigation through diversity reception.

In the following, we will highlight the contributions of remote control, remote modulation and channel sounding to the operation of the FSO link.

A. Focal Plane Array Beamformer

The layout of the FSO terminals is shown in Fig. 2(b). The air interfaces of these terminals build on a FPA configuration to ensure simple control and calibration for defining the emitted pencil beams. The emission direction of the beams is defined by introducing an offset for the optical signal launch with respect to the focal center of the collimation lens. This is achieved through implementing an antenna element plane at the tip of the launch fiber by means of a photonic lantern, whose launch waveguide is then defined through a beamforming network based on either optical space switching or through spectral routing. The specifics of this FPA concept have been reported in [19]. In this work, we use a photonic lantern with an extended number of 91 single-mode cores that feature a mode-field diameter of 8.4 µm. These cores are hexagonally arranged over the cross-section of the focal antenna plane with a spacing of $\pi = 35 \mu m$ and up to N = 11launch cores per axis. The worst-case crosstalk among cores is less than -47 dB, while the fill factor for all cores over the focal plane is 5.9% or -12.2 dB. A single 2" lens with a focus of f = 100 mm serves the beam collimation, for which a diameter of ~28 mm is yielded for FSO propagation. Furthermore, the field-of-view that results from this optical setup, which is yielded by $FoV = N \cdot \pi / f = 0.22^{\circ}$, is sufficiently wide for stationary point-to-point links that do not foresee

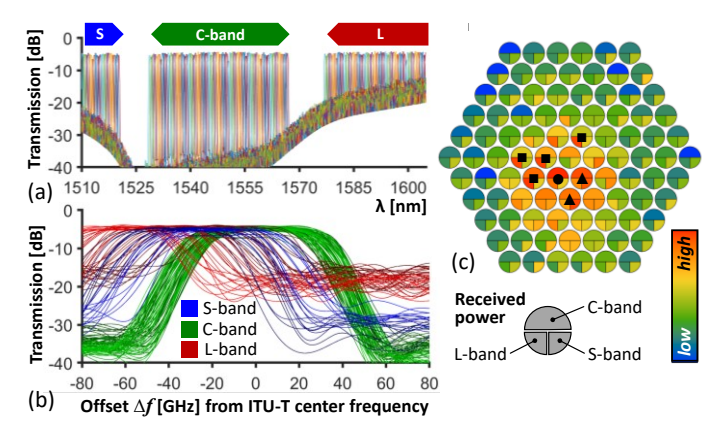


Fig. 4. Spectral uniformity for a 1×96 single-waveband AWG. (a) Channel transmission, (b) channel overlap in multiple wavebands, (c) received power at focal plane.

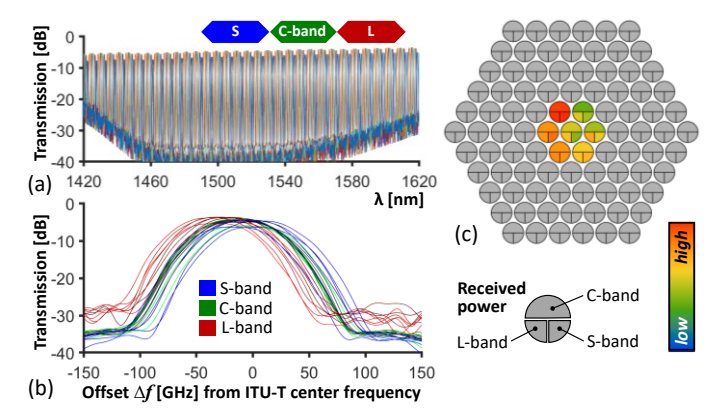


Fig. 5. Spectral uniformity for an 8×8 multi-band AWG. (a) Channel transmission, (b) channel overlap in multiple wavebands, (c) received power at focal plane.

mobility for its terminals. In order to enable bidirectional transmission, an angled (8°) polish has been applied to the end-facet of the focal plane. Optical space switching and spectral routing are facilitated by an optical switch (SWI) based on micro-electro-mechanical system (MEMS) technology and through a (cyclic) arrayed waveguide grating (AWG) at the HE- and TE-side FSO terminals, respectively. The passive wavelength routing scheme with fixed wavelength allocation per antenna element for the TE-side beamforming network enables centralized link control, as indicated in Fig. 2(b) where a tunable source selects the TE-side antenna element by means of simple choice of its emission wavelength.

B. Remote Control and Modulator Seeding

Simplification of the TE terminals is driven by adopting remote control and remote modulation – two notions that centralize network intelligence and ease resource management. The first is accomplished through a wavelength-routing architecture of the TE-side FPA, which enables the centralized HE to remotely orchestrate the FPA at the TE through simple wavelength choice: While the TE-side antenna element can be directly selected through the wavelength of the data signal, the HE-side beamforming network has been laid

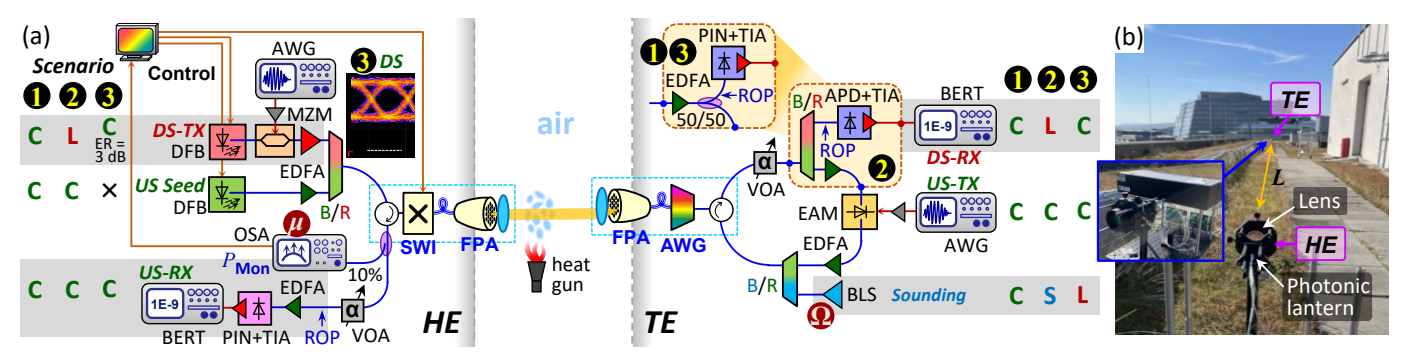


Fig. 6. (a) Experimental setup of the FSO link for the three chosen implementation scenarios. (b) Out-door FSO link setup.

out in a space-switched and thus colorless fashion.

The second notion is implemented through use of a polarization-insensitive electro-absorption modulator (EAM) as the US transmitter at the TE. This source-less modulator is remotely seeded by the HE, which mitigates complex and precise spectral control that would be required for a locally sourced TE transmitter. Moreover, the overall synchronization among network resources is greatly relaxed since no element needs to be actively switched in either spatial or spectral dimension. As a prerequisite for this implementation, the EAM transmitter is required to feature a colorless response within the (US) data transmission waveband – which in case of the present experiment has been dedicated to the C-band for all scenarios. Figure 3 reports the wavelength-specific transmission characteristics of the EAM as a function of its bias voltage $V_{\rm EAM}$. The static modulation extinction ratio ε , which is shown for a swing of 2 V_{pp}, remains larger than 11.6 dB over the entire wavelength range of interest, which is defined over $\lambda = [1528.77, 1564.68]$ nm. Even though the fiber-to-fiber insertion loss at $V_{\rm EAM} = 0$ V increases to 15.1 dB at $\lambda = 1528.77$ nm, this increased loss can be accounted for during optical re-amplification at the TE terminal. It shall be noted that specifically designed wideband EAMs [23] should be employed for the proposed application.

C. Simultaneous Channel Sounding

Acquisition of the channel conditions provides information for centralized beamforming on the best available channel transmission among all FPA elements. Given the cyclic response of the AWG as beamforming network at the TE, the injection of white light over the FSO link will introduce a coupling-dependent signature for all its antenna elements over all wavebands, which can be easily retrieved through simple spectral monitoring at the HE. With this, the optimal antenna element pair can be determined to optimize the FSO channel transmission and the DS and US seed wavelengths at the HE can be tuned accordingly.

To enable a spectrally repeated imprint of the FSO link quality at the S-, C- and L-bands, information must be correctly replicated across these adjacent wavebands, by virtue of its cyclic response that covers an extended spectral range including the adjacent wavebands. This further implies that the involved AWG has a uniform channel spacing over multiple wavebands. Figure 4(a) presents the transmission function of

the 96 channels of a single-band 1×96 AWG with a 50 GHz spacing over the C-band, together with the transmission in the adjacent S- and L-bands. When collapsing all channels over a reference ITU-T grid with 100-GHz spacing while offsetting the 48 interleaved channels by 50 GHz, we see a good overlap in channel transmissions within the C-band. This is evidenced in Fig. 4(b) by the overlap in rising and falling -3dB channel edges at an offset $\Delta f = +26/-24$ GHz from the ITU-T channel center. However, this uniformity does not apply for the adjacent wavebands, which show a wide spread in channel frequencies due to a spatial dispersion of the frequencies at the output plane of the single-band AWG [24]. As a result of this effect, information obtained through sounding at an adjacent waveband is related to a different antenna element of the FPA. This is shown in Fig. 4(c) in terms of received power over all antenna elements in the target C-band and the two adjacent monitoring S- and L-bands. While the monitoring bands do point to the right group of antenna elements, neither of them indicates the optimal antenna element (•). Spatial averaging between the high-return elements in the S- (▲) and L-band (■) can improve the pinpointing of the correct antenna element – despite the poor channel uniformity of the utilized AWG.

For comparison, Figure 5(a) shows the transmission of a dedicated multi-band 8×8 AWG with 100 GHz spacing and no skip channels in its cyclic response. The channel transmission functions show a much smaller shift Δf to the nominal center frequency. Figure 5(b) proves this through an average shift of +6 and -31 GHz for the S- and L-bands, respectively. Consequently, the antenna elements at the focal plane feature a higher correlation in received power at the adjacent wavebands, as reported in Fig. 5(c). It shall be noted that the reduced number of eight AWG ports restricts an investigation to a smaller number of antenna elements, for which the seven innermost elements of the focal plane have been chosen.

III. EXPERIMENTAL FSO SETUP

The FSO link has been evaluated in the experimental setup presented in Fig. 6(a). The DS was modulated on an optical carrier wavelength determined by the actual scenario. A Mach-Zehnder modulator (MZM) is employed for this purpose. It is combined with the US seed wavelength through a blue/red (B/R) waveband splitter while the US seed is omitted for the case of wavelength re-use (3), for which the

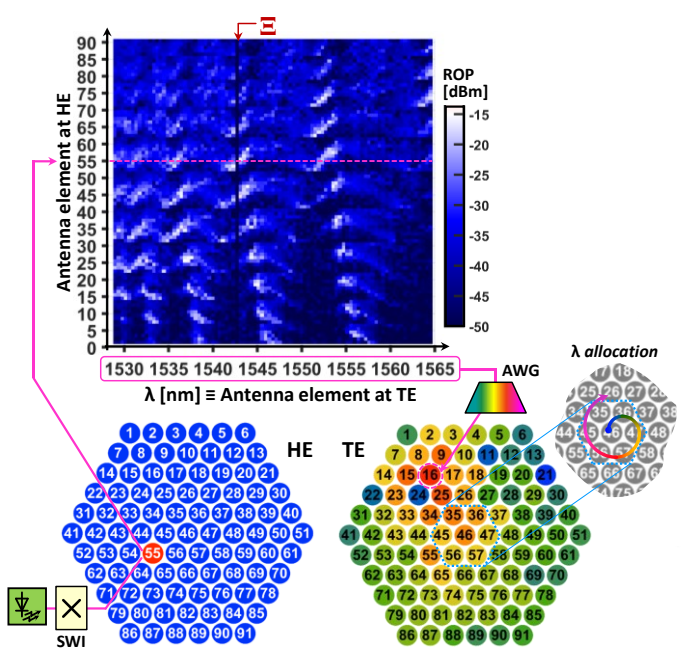


Fig. 7. Optical coupling between the HE- and TE-side air interfaces. The focal planes exemplarily show the TE-side received power distribution for a launch at the HE antenna element 55.

DS is instead transmitted with a reduced ER of 3 dB. The HE then launches these signals over the space-switched FPA beamformer over either an in-door lab link with a distance of 6 m or an out-door link over a distance of L = 63 m, which is shown in Fig. 6(b). Due to the limits of the employed components, we were not able to exceed data rates of 10 Gb/s, while in principle the use of high-bandwidth electro-optics permits single-channel data rates beyond 50 Gb/s [25].

At the TE the signal is coupled to a single-mode fiber through the wavelength-routed FPA beamformer. It enters a re-modulation loop that includes the aforementioned EAM-based US transmitter, which is accompanied by optical amplifiers to condition the signal level. For the DS reception, the TE builds on an avalanche photodetector (APD) with cointegrated transimpedance amplifier (TIA) after waveband splitting in case that a dedicated DS waveband is employed (2). In the other two implementation scenarios that target half-duplex operation (1) or wavelength re-use (3), the optically pre-amplified signal is split off before the EAM transmitter by a 50/50 coupler for subsequent photoreception with a simpler PIN+TIA receiver.

The US signal is combined with the sounding signal (2,3) that originates from a broadband light source in the respective waveband. It is then launched back to the HE through the FPA beamformer. The required directional split at each of the FSO terminals is realized through optical circulators. At the HE, an optically pre-amplified PIN+TIA receiver is employed to detect the US signal. Variable optical attenuators (VOA) have been included at the HE and TE to evaluate the transmission quality through real-time bit error ratio (BER) testing as a function of the received optical power

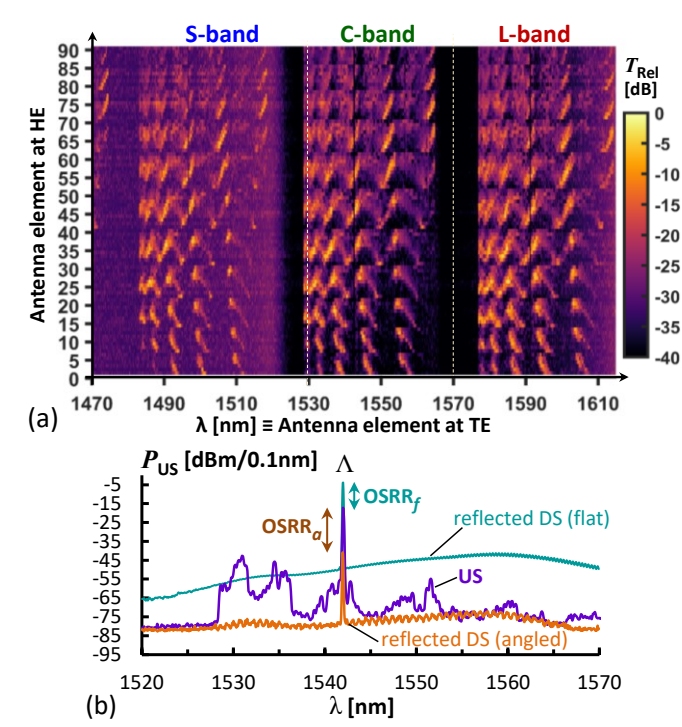


Fig. 8. (a) Channel sounding over multiple wavebands that range from the S- to the L-band. (b) Received spectrum at HE for angled and flat polish of the photonic lantern at the HE-side FPA beamformer.

(ROP).

IV. CHARACTERIZATION OF THE FSO LINK

A. Optical Coupling between Air Interfaces

The optical coupling over the FSO channel is first evaluated according to the channel conditions when establishing links for different antenna elements at the HE and TE beamformers. For scenario ①, this procedure is to be performed prior to data transmission and will have to be periodically repeated to maintain optimal coupling between the terminals.

Figure 7 presents an example for the in-door FSO links by reporting the established optical coupling conditions between all HE- and TE-side FPA antenna elements. For this, the antenna elements at the TE are referenced to their actual spectral channel λ that results from its wavelength-routed FPA architecture. This allocation between wavelength domain and spatial coordinate of the antenna element at the focal plane follows a spiral-shaped inwards-out assignment of the 50-GHz spaced AWG channels, as it is indicated at the inset of Fig. 7. For the provided example, the launch of the HE-side signal at antenna element 55 results in an optimal coupling with a received power of -13.2 dBm at the antenna element 16 of the TE, corresponding to a signal wavelength of $\lambda = 1542.89$ nm. This is evidenced by the power distribution of the two focal planes that have been appended to Fig. 7 for this launch condition. It shall be noted that the exceptionally poor coupling that is marked by Ξ in Fig. 7 is solely caused by a faulty fiber port at the TE-side photonic lantern, specifically impacting the FPA antenna element 24.

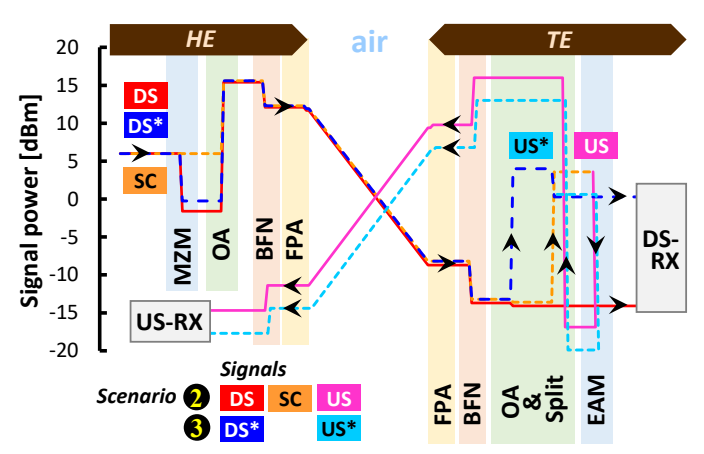


Fig. 9. Signal evolution along the bidirectional FSO link. Power levels are shown for the DS, the seed and the US signals of scenarios 2 and 3.

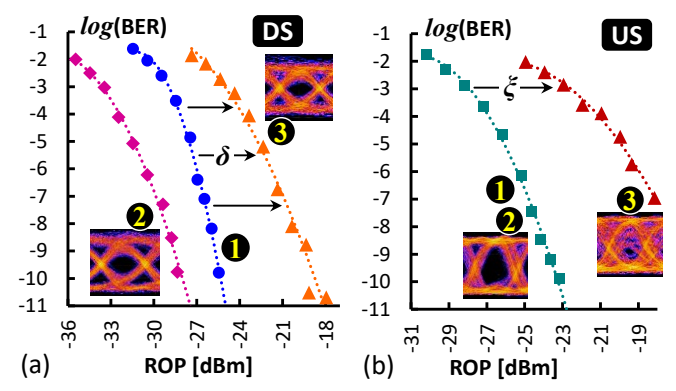


Fig. 10. BER performance of the 10 Gb/s (a) DS and (b) US.

B. FSO Channel Sounding

In case of scenarios 2 and 3, we utilize additional spectral wavebands. Since we dedicate only one or two wavebands to full-duplex data transmission, the other band(s) are available for the purpose of channel sounding. As introduced in Section II.C, this enables us to perform continuous monitoring of the link conditions and to optimize the optical coupling between the HE- and TE-side FSO terminals accordingly.

Figure 8(a) shows this functionality through the wideband S+C+L spectrum that is acquired at the HE monitor (μ in Fig. 6) upon white-light injection at the TE (Ω). The information obtained from the adjacent wavebands resemble the coupling conditions reported in Fig. 7, pending minor AWG-specific corrections as discussed in Section II.C. It shall be stressed that the reduced contrast in the S-band is a result of the limited emission power of the white-light source in this spectral window.

Figure 8(b) reports the optical spectrum of a C-band US signal at $\Lambda=1541.97$ nm, as acquired by the HE. This US has been recorded for scenario 3, meaning that it has been remotely seeded by the HE through re-use of the DS signal as the optical US carrier. This "reflective" seeding scheme necessitates a high optical return loss for several FPA elements. Compared to the reflected DS signature that is

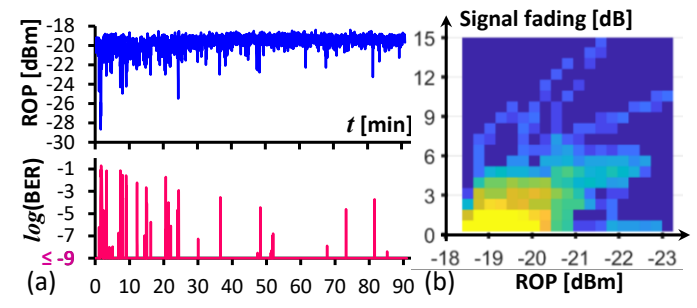


Fig. 11. (a) Long-term BER and ROP acquisitions for the outdoor FSO link setting and (b) correlation between the fading in recorded signal envelope and ROP.

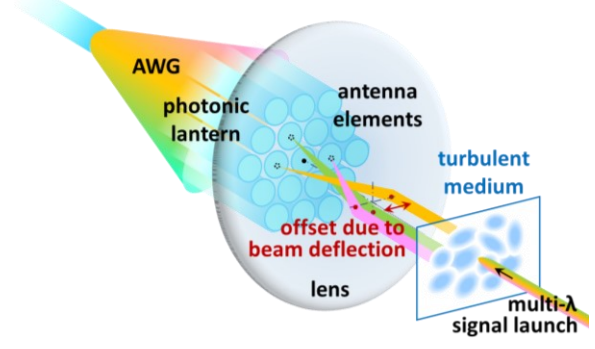


Fig. 12. Diversity reception through data transmission on a wavelength-set.

received at the US receiver at the HE when deliberately blocking the FSO link, the actual US signal is strong enough to ensure a high optical signal-to-reflection ratio (OSRR) of $OSRR_a = 23.4$ dB for US reception during bidirectional operation of the FSO link. This high value is enabled by the angled polish at the FPA aperture. Figure 8(b) further shows a DS signature when omitting the angled polish and when instead using a 61-port photonic lantern with flat end-facet. Here, the crosstalk due to a too low $OSRR_f$ of -13.5 dB would spoil any US reception, even under remote seeding (scenario 2) due to strong carrier-carrier beating.

C. Signal Evolution along the Bidirectional FSO Link

The evolution of the signal power along the bidirectional FSO link is reported in Fig. 9. Shown are the L-band DS, the optical C-band seed carrier (SC) and the resulting C-band US for scenario 2 and the C-band DS* and US* for scenario 3 where wavelength re-use is employed. The signals are sourced at the HE with 6 dBm. Measurements have been taken after data modulation with the MZM at the scenario-specific intensity modulation index, after subsequent power boosting through optical amplification (OA) and the pass-through at the FSO terminal involving the beamforming network (BFN) and the FPA. At the HE, the signal(s) are launched with 11.9 dBm into the FSO channel. At the TE, the delivered signal is reconditioned by means of OA and the DS and US lightpaths are separated before re-modulation with the EAM. The signal power is kept above -20 dBm at any point of the signal chain and eventually launched with 9.4 dBm over the FSO link

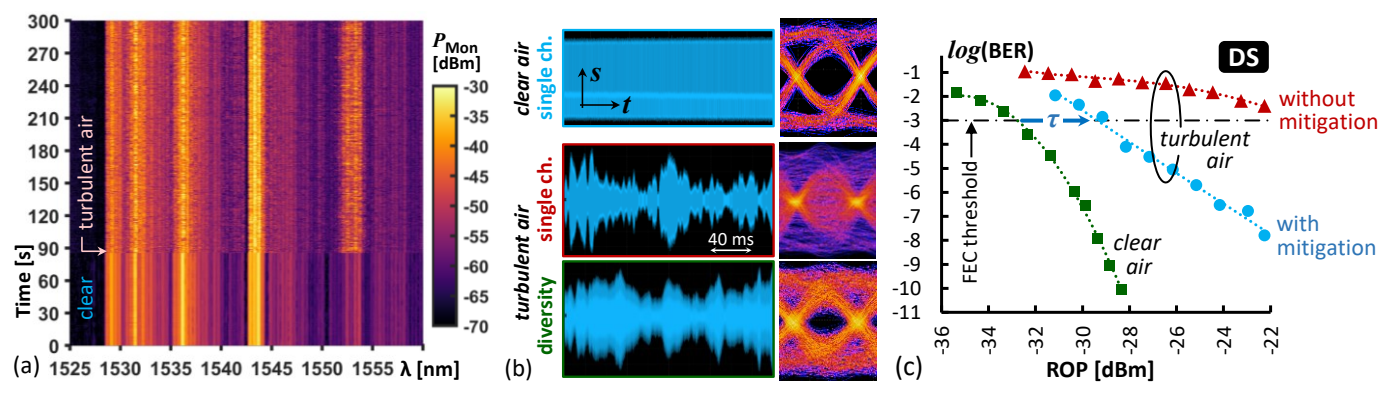


Fig. 13. (a) Turbulence-induced power spread in sounded FSO coupling and (b) resulting fading in signal envelope and DS eye diagram. (c) BER performance under clear-air conditions and in presence of turbulence, without and with mitigation.

TABLE II
WAVELENGTH-SET ALLOCATION TO MITIGATE TURBULENCE.

Set element	Antenna element at TE	Wavelength [nm]
1		1542.25
1	9	1543.25
2	10	1543.73
3	16	1542.89
4	17	1536.24
5	18	1536.60
6	25	1535.89
7	26	1531.49

towards the US receiver at the HE.

V. DATA TRANSMISSION PERFORMANCE

Figure 10 presents the data transmission performance for the in-door FSO link in terms of BER measurements. For the 10 Gb/s DS, reported in Fig. 10(a), reception sensitivities of -25.4 dBm (•) and -18.8 dBm (▲) are accomplished at a BER of 10⁻¹⁰ for the C-band layout in scenarios **1** and **3**, that employ the EDFA+PIN receiver configuration at the TE and intensity modulation ERs of >10 dB and 3 dB, respectively. The average sensitivity penalty of 5.2 dB (δ) over the BER curve in the wavelength re-use scenario 3 agrees well with the expected value of 4.8 dB [22] due to the reduced eye opening if the DS ER is reduced to 3 dB at the HE transmitter to enable full-duplex transmission over a single wavelength. The L-band DS of scenario 2, which is detected with an APD receiver, further benefits from the additional optical noise filtering through the AWG right before downstream reception at the TE. The obtained sensitivity is -28 dBm at a BER of 10^{-10} (\blacklozenge), which resembles the sensitivity of the utilized APD receiver and thus indicates that no additional degradation is incurred.

The BER performance of the 10 Gb/s US is presented in Fig. 10(b). For remotely seeding the US transmitter with a continuous-wave signal as intended in scenarios \bullet and \bullet , a sensitivity of -23.2 dBm (\bullet) is accomplished at a BER of 10^{-10} . A penalty of 5.3 dB (ξ) is incurred at the FEC level of 10^{-3} when the DS is used as optical US carrier (\bullet) in scenario \bullet 3. This penalty could be further reduced when adopting DS suppression techniques suitable for symmetric data rates [22].

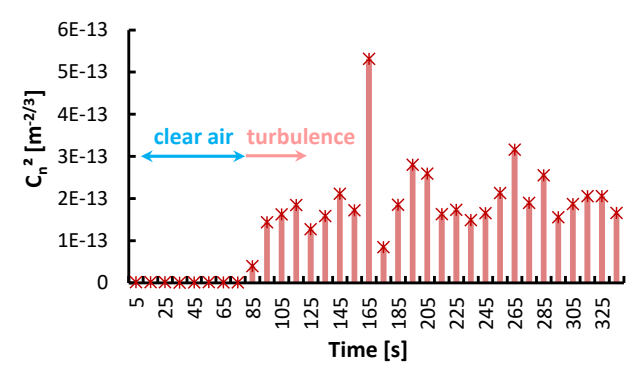


Fig. 14. Refractive index structure parameter for 10-second time intervals before and after inducing turbulent conditions.

The FSO setup has then been transferred to the roof-top location shown in Fig. 6(b), in order to expose the link to more realistic deployment conditions. The corresponding BER for DS transmission in scenario 1 has been continuously acquired over 90 minutes on a sunny autumn day that is characterized by an average solar irradiance of 49 klux and a temperature of 13.9°C. The result of this real-time BER testing is reported in Fig. 11(a). The vast majority of 97.3% of the BER acquisitions were found to fall below a level of 10⁻⁹. However, we noticed several excursions in the acquired BER that are accompanied by a fast fading in ROP. This is attributed to windy weather conditions during the first part of the measurement. Figure 11(b) shows this correlation between the signal fading in the simultaneously monitored signal envelope and the recorded ROP. These fluctuations are too fast to be compensated by means of beamforming due to the slow response in optical switching and spectral tuning of the source laser. This inevitably results in deep fading for the received signal unless additional means of turbulence mitigation are employed.

VI. MITIGATION OF OPTICAL TURBULENCE

According to the FPA principle employed for free-space to fiber coupling, optical turbulence causes a loss in coupling since the beam is diverted to other antenna elements on a time scale that is too fast to actively track. However, since we know the assignments of adjacent antenna elements and given the

spectral nature of these assignments, a set of wavelengths can be launched to ensure that optimal coupling conditions are maintained under the impact of turbulence, similar as it would apply to a reception diversity scheme. This principle is sketched in Fig. 12. As the light beam passes through turbulent air, a lateral offset is introduced to the FSO beam. By expanding the DS to a wavelength-set that matches the adjacent antenna elements of the currently set element that is expected to yield the optimal coupling conditions under clearair conditions, the effect of turbulence can be greatly reduced through simple incoherent power combining of the (partially) received wavelength-set. This recovers the drop in signal power due to fading, given that all the wavelengths of the launched set are modulated by the same DS signal.

The effectiveness of the proposed turbulence mitigation scheme has been evaluated for the in-door FSO channel that has been actively perturbed by artificially introduced turbulence. Specifically, a heat gun set to 600°C and aimed at the beam launch directly in front of the HE-side FPA aperture has been used for this purpose. Figure 13(a) presents the effect of turbulence on the information recorded through channel sounding. We calculated the Rytov variance σ_1^2 from the fluctuations of the received optical power as described in detail in [26, 27], taking aperture averaging into account. The resulting σ_{1}^{2} fulfills the conditions for moderate turbulence $(\sigma_1^2 \le 0.3)$. Moreover, we subsequently estimated the refractive index structure parameter C_n², which is shown in Fig. 14. It shows a distinct increase in turbulence once the heat gun is activated and features an average value of 2×10⁻¹³ m^{-2/3} when inducing turbulent conditions to the free-space channel.

In presence of turbulence, the coupled power spreads from the previously optimal channel to multiple adjacent antenna elements. With this, the acquired 10 Gb/s DS waveform, which is presented in Fig. 13(b), now shows strong fading and a closed eye diagram when compared to the constant signal envelope and open eye diagram under clear-air conditions. As Fig. 13(c) confirms, the resulting BER under turbulence shows a high error floor larger than 10^{-3} (\blacktriangle) and thus beyond hard-decision forward error correction (FEC) capabilities for this single-wavelength DS launch.

We then expanded the DS launch to a wavelength-set configured to cover the adjacent antenna elements of the current setting to enable diversity reception. This wavelengthset therefore covers seven wavelength channels, as presented in Table II. The beneficial effect is directly visible from the resulting signal envelope and the re-opening of the eye diagram. The corresponding BER performance (•) confirms the effectiveness of the proposed mitigation scheme through operation well below the FEC limit. This means that 10 Gb/s DS transmission can be again accomplished in presence of turbulence. Despite the residual penalty of 3.4 dB (τ) that is incurred in comparison to clear-air conditions () and caused by, e.g., architectural limitations such as the spacing of the antenna elements, a large power margin of 7.2 dB remains for the operation of the FSO link. It can be expected that the diversity gain is maintained when the number of beamformer

elements is scaled up since the number of neighboring elements, and thereby the size of the wavelength set, remains constant.

VII. CONCLUSION

We have demonstrated a bidirectional point-to-point FSO link for full-duplex 10 Gb/s transmission employing FPA beamformers with 91 antenna elements for optimization of the Fi-Wi-Fi coupling between two single-mode fiber ports and simultaneous channel sounding. The reflective design of the terrestrial FSO bridge simplifies the tail-end terminal by providing a source-less design and centralized control. Various spectral configurations have been evaluated for accomplishing full-duplex 10 Gb/s transmission and continuous link quality estimation at the same time. On top of this, the flexibility of the wavelength-routed FPA architecture has been exploited for the purpose of turbulence mitigation, which has been successful demonstrated by means of diversity reception as it results from a simple expansion of singlewavelength data transmission to an incoherently combined wavelength-set.

REFERENCES

- S.A. Al-Gailani et al., "A Survey of Free Space Optics (FSO) Communication Systems, Links, and Networks," *IEEE Access*, vol. 9, pp. 7353-7373, 2020.
- [2] C.W. Chow, "Recent Advances and Future Perspectives in Optical Wireless Communication, Free Space Optical Communication and Sensing for 6G," J. Lightwave Technol., vol. 42, no. 11, pp. 3972-3980, 2024.
- [3] P.A. Hoeher, J. Sticklus, and A. Harlakin, "Underwater Optical Wireless Communications in Swarm Robotics: A Tutorial," *IEEE Comm. Surveys & Tut.*, vol. 23, no. 4, pp. 2630-2659, 2021.
- [4] C. Schieler et al., "On-orbit demonstration of 200-Gbps laser communication downlink from the TBIRD CubeSat," in Proc. SPIE Photonics West LASE, San Francisco, United States, Jan.-Feb. 2023, vol. 12413, art. no. 1241302.
- [5] M. Fernandes et al., "4 Tbps+ FSO Field Trial Over 1.8 km With Turbulence Mitigation and FEC Optimization," J. Lightwave Technol., vol. 42, no. 11, pp. 4060-4067, 2024.
- [6] V. van Vliet, M. van den Hout, K. Gumus, E. Tangdiongga, and C. M. Okonkwo "5.7 Tb/s Transmission Over a 4.6 km Field-Deployed Free-Space Optical Link in Urban Environment," in *Proc. Opt. Fiber Comm. Conf. (OFC)*, San Francisco, United States, Mar.-Apr. 2025, paper M2J.7.
- [7] H. Zhou et al., "Demonstration of 1.024-Tbit/s 16-Channel Mid-IR FreeSpace Optical Communications by Combining Wavelength, Polarization, and Mode Multiplexing," in Proc. Opt. Fiber Comm. Conf. (OFC), San Francisco, United States, Mar.-Apr. 2025, paper Th4A.6.
- [8] K. Newell, M.P. O'Toole, and K. Patel, "Free-Space Optical Link Between Two Ships at Sea," in *Proc. Europ. Conf. Opt. Comm.* (ECOC), Frankfurt, Germany, Sep. 2024, paper W1D.5.
- [9] D.R. Kolev *et al.*, "Latest Developments in the Field of Optical Communications for Small Satellites and Beyond," *J. Lightwave Technol.*, vol. 41, no. 12, pp. 3750-3757, 2023.
- [10] "NASA's tech demo streams first video from deep space via laser," Jet Propulsion Laboratory / NASA, Dec. 2023, online available at: https://go.nasa.gov/47XDYom
- [11] M.A. Khalighi, and M. Uysal, "Survey on Free Space Optical Communication: A Communication Theory Perspective," *IEEE Comm. Surveys & Tut.*, vol. 16, no. 4, pp. 2231-2258, 2014.
- [12] A.I. Martinez et al., "Self-adaptive integrated photonic receiver for turbulence compensation in free space optical links," Sci. Rep., vol. 14, art no. 20178, 2024
- [13] K. Xu et al., "FPGA-Based Real-Time Mode-Diversity Coherent Reception Experiment Over a 15.6 km Horizontal Turbulence Link," in

- Proc. Opt. Fiber Comm. Conf. (OFC), San Francisco, United States, Mar.-Apr. 2025, paper M4G.6.
- [14] M. Guo et al., "Low-complexity 24-h 29-km inter-island real-time FSO communication under strong turbulences," Opt. Lett., vol. 50, no. 2, pp. 546, 540, 2025.
- [15] Y.H. Jian, T.Y. Hung, D. Yi, H.K. Tsang, and C.W. Chow, "Enhanced Atmospheric Turbulence Resiliency in Free Space Optical Communication (FSOC) With MIMO Programmable Silicon-Photonics Processor," in *Proc. Opt. Fiber Comm. Conf. (OFC)*, San Francisco, United States, Mar.-Apr. 2025, paper M4G.4.
- [16] Z. Pan, Y. Li, Y. Shen, Z. Li, G. Huang, C. Geng, and X. Li, "Multi-Aperture Adaptive Fiber-Coupled Free-Space Optical Communication System: Scintillation Mitigation and Turbulence Compensation Experiment Based on Gamma-Gamma Channel Modeling," *Phot. J.*, vol. 17, no. 2, art. no. 7300807, 2025.
- [17] Y. Li et al., "Enhanced Atmospheric Turbulence Resiliency With Successive Interference Cancellation DSP in Mode Division Multiplexing Free-Space Optical Links," J. Lightwave Technol., vol. 40, no. 24, pp. 7769-7778, 2022.
- [18] F. Honz, and B. Schrenk, "Bidirectional and Turbulence-Resilient Fi-Wi-Fi Bridge", in *Proc. Opt. Fiber Comm. Conf. (OFC)*, San Francisco, United States, Mar.-Apr. 2025, paper M4G.3.
- [19] F. Honz, and B. Schrenk, "Alignment-Tolerant Optical Fi-Wi-Fi Bridge Assisted by a Focal Plane Array Beamformer as Air Interface", J. Lightwave Technol., vol. 43, no. 13, pp. 6187-6193, DOI: 10.1109/JLT.2025.3553914.
- [20] A. Fayad, T. Cinkler, and J. Rak, "Toward 6G Optical Fronthaul: A Survey on Enabling Technologies and Research Perspectives," *IEEE Comm. Surveys & Tut.*, vol. 27, no. 1, pp. 629 - 666, 2025.
- [21] M. Z. Chowdhury, M. K. Hasan, M. Shahjalal, M. T. Hossan, and Y. M. Jang, "Optical Wireless Hybrid Networks: Trends, Opportunities, Challenges, and Research Directions," *IEEE Commun. Surv. Tutor.*, vol. 22, no. 2, pp. 930-966, 2020. DOI: 10.1109/COMST.2020.2966855.
- [22] B. Schrenk et al., "All-Optical Carrier Recovery Scheme for Access Networks with Simple ASK Modulation," J. Opt. Comm. and Netw., vol. 3, no. 9, pp. 704-712, Sept. 2011.
- [23] Y. Liu et al., "Thermally tunable GeSi electro-absorption modulator with a wide effective operating wavelength range," Phot. Res., vol. 11, no. 8, pp. 1474-1483, 2023.
- [24] P. Muñoz, D. Pastor, and J. Capmany, "Modeling and Design of Arrayed Waveguide Gratings," J. Lightwave Technol., vol. 20, no. 4, pp. 661-674, 2002.
- [25] Z. Liu et al., "56 Gbps high-speed Ge electro-absorption modulator," Photon. Res., vol. 8, no. 10, pp. 1648-1652, 2020. DOI: 10.1364/PRJ.401140.
- [26] A. Tunick, "Optical turbulence parameters characterized via optical measurements over a 2.33 km free-space laser path," *Opt. Expr.*, vol. 16, no. 19, pp. 14645-14654, 2008.
- [27] A. Arockia Bazil Raj, J. Arputha Vijaya Selvi, and S. Durairaj, "Comparison of different models for ground-level atmospheric turbulence strength (C_n^2) prediction with a new model according to local weather data for FSO applications," *Appl. Opt.*, vol. 54, no. 4, pp. 802-815, 2015.